

Impact of horizontal resolution in CALMET on simulated near-surface wind fields over complex terrain during Super Typhoon Meranti (2016)



Shengming Tang^{a,b}, Sui Huang^c, Hui Yu^{a,b,*}, Ming Gu^d, Jie Tang^a

^a Shanghai Typhoon Institute of China Meteorological Administration, Shanghai 200030, China

^b Key Laboratory of Numerical Modeling for Tropical Cyclones, China Meteorological Administration, Shanghai 200030, China

^c Guangdong Kenuo Surveying Engineering Co., LTD, Guangzhou 510663, China

^d State Key Laboratory for Disaster Reduction in Civil Engineering, Tongji University, Shanghai 200092, China

ARTICLE INFO

Keywords:

CALMET
Horizontal resolution
Complex terrain
Typhoon Meranti
Slope angle

ABSTRACT

A Weather Research and Forecasting (WRF) model simulation with 3-km horizontal grid spacing was coupled with five California Meteorological Model (CALMET) simulations with horizontal grid spacing ranging from 100 m to 3 km to investigate the impact of horizontal resolution on the simulated near-surface wind fields of Super Typhoon Meranti (2016). Assessment of the model output was conducted in two specified regions named Shisun Mountain and Shishe Mountain in Fujian Province, China. The WRF/CALMET coupled system exhibited satisfactory performance, as indicated by the reasonably large correlation coefficient (> 0.4) between the simulated and observed winds. The best and second-best outcomes for 10-m wind speed were found in the simulations with horizontal grid spacing of 500 and 250 m, respectively. Specifically, the 10-m wind speed appeared sensitive to model resolution after being affected by the gale-force winds of Typhoon Meranti. For the 10-m wind direction, the best outcome at Shisun Mountain was found with 500-m horizontal grid spacing, whereas it improved continuously with higher horizontal resolution at Shishe Mountain. The wind-followed slope angle was proposed to provide new perspective for quantitative evaluation of the impact of complex terrain with different horizontal resolutions on the near-surface wind field. It is found that, irrespective of the location and model resolution, the 10-m downhill winds were generally larger than the uphill winds before and after being affected by the gale-force winds, while the winds decreased with slope angle in both uphill and downhill situation when affected by the gale-force winds of Typhoon Meranti.

1. Introduction

Tropical cyclones are one of the most destructive natural phenomena in the world. In mainland China, the main disaster-causing factors of tropical cyclones are wind gusts, rainstorms and storm surges (Chen et al., 2019). On the one hand, wind is an important variable in various fields such as civil engineering, wind energy assessment, air pollutant dispersion and transportation systems. On the other hand, wind is also considered one of the most difficult meteorological variables to reproduce and to predict owing to its dependence on the specific characteristics of any given location such as topography, surface roughness and surface coverage (Morales et al., 2012).

Commonly, wind speed is characterized through in situ observation. However, obtaining such measurements is often affected by certain constraints and limitations, and the instruments required are normally costly and distributed sparsely with coarse resolution (Al-Yahyai et al.,

2010). Therefore, one feasible solution for the determination of wind speed is to use different types of numerical simulation. For instance, various models exist that differ in terms of characteristics such as numerical formulation, assumptions, equation simplifications and type (i.e., prognostic or diagnostic models) (Morales et al., 2012). Prognostic models solve equations that describe atmospheric processes and predict how the atmosphere might change with time. Typically, numerical weather prediction models, especially mesoscale area-limited models such as the fifth-generation nonhydrostatic Pennsylvania State University–National Center for Atmospheric Research mesoscale model (MM5; Grell et al., 1995), Weather Research and Forecasting (WRF) model (Skamarock et al., 2008) and the High-resolution Regional Model (HRM; Majewski, 2009), are used for the calculation of wind fields with horizontal resolution of several kilometers. By contrast, diagnostic models represent the actual state of the atmosphere and address smaller-scale topographic effects with much finer resolution (Hu

* Corresponding author at: Shanghai Typhoon Institute of China Meteorological Administration, Shanghai 200030, China.

E-mail address: yuh@typhoon.org.cn (H. Yu).

et al., 2010). Typical examples of diagnostic models are the Wind Atlas Analysis and Application Program (WAsP; Mortensen and Landberg, 1993), Mass Consistent model associated with the Second-order Closure Integrated Puff model (MCSCIPUF; Sykes et al., 1998), California Meteorological model (CALMET; Scire et al., 1998) and the Regular Meteorological Preprocessor Program of the U.S. Environmental Protection Agency (AERMET; US EPA, 2004). Recently, it has become increasingly common for diagnostic models to be run in association with prognostic models to generate high-resolution wind fields with horizontal resolution of several hundred meters. One of the most prominent examples is the WRF/CALMET coupled system that generates wind fields over complex terrain. The CALMET/CALPUFF (California Puff) modeling system (Exponent, Inc., Dallas, TX, USA) is commonly used around the world in evaluations of the impact on air quality, including the calculations of air pollution dispersion to great distances and over complex terrain (Oleniacz and Rzeszutek, 2018). During the past two decades, the CALMET model has been evaluated repeatedly and found valid in stable weather conditions when the wind field is quasi-nondivergent (Jackson et al., 2006; Yim et al., 2007; Gioli et al., 2014; Rood, 2014; Oleniacz and Rzeszutek, 2018).

Because the simulation results of tropical cyclones are generally considered sensitive to model resolution (Fierro et al., 2009; Gopalakrishnan et al., 2011; Kanada and Wada, 2016), it is of great importance to study the impact of different horizontal resolutions on CALMET-simulated wind fields over complex terrain. Chandrasekar et al. (2003) evaluated the performance of the MM5/CALMET coupled system around the New Jersey and Metropolitan Philadelphia region (USA). The wind field outputs from the 36-, 12- and 4-km MM5 models were ingested into the CALMET model with 4-km horizontal resolution. Very small differences were found in the horizontal wind components between the CALMET predictions at the three horizontal resolutions. Lu et al. (2012) examined CALMET near-surface winds with 100-m horizontal spacing that were driven by the outputs from the WRF model with 3- and 1-km horizontal spacing over a coastal island with complex topography. The correlation coefficient indicated no corresponding improvement when the grid spacing decreased from 3 km to 100 m. For an area of complex terrain in Spain, Gonzalez et al. (2015) evaluated the results of CALMET at three different horizontal resolutions (200 m, 500 m and 1 km), which were nested to WRF model simulations with 3-km horizontal resolution. The surface performances of the three simulations with differing horizontal resolution were similar, showing that CALMET could not improve the WRF results without incorporating actual measurements. Rzeszutek (2019) evaluated the CALMET/CALPUFF model in near-field and complex terrain by changing the grid resolution across a wide range, i.e., 100–4000 m. It was noted that horizontal resolution of approximately 250 m (or less) is recommended for use on local-scale and complex terrain in CALMET. However, it was found that the best outcomes in terms of CALMET/CALPUFF accuracy were achieved for 400-m grid resolution. The above studies are reviewed here briefly to illustrate the sensitivity of CALMET results to model resolution in stable weather conditions over complex terrain. However, in unstable conditions such as tropical cyclones, the impact of differing horizontal resolution on CALMET-simulated wind fields is usually neglected.

This paper presents an assessment of the impact of the horizontal resolution in the CALMET model on the wind fields of diagnostic modeling in two specified mountains characterized by single-peak and double-peak structures during the passage of Super Typhoon Meranti in 2016. The mesoscale WRF model was employed to provide an initial guess wind field over the typhoon-affected region, and five CALMET simulations with horizontal grid spacing ranging from 100 m to 3 km were conducted to resolve the microscale terrain effects. In particular, compared with traditional statistical scores, the conventional slope angle is redefined herein to provide new perspective for quantitative evaluation of the impact of complex terrain with different horizontal resolutions on the simulated near-surface wind field.

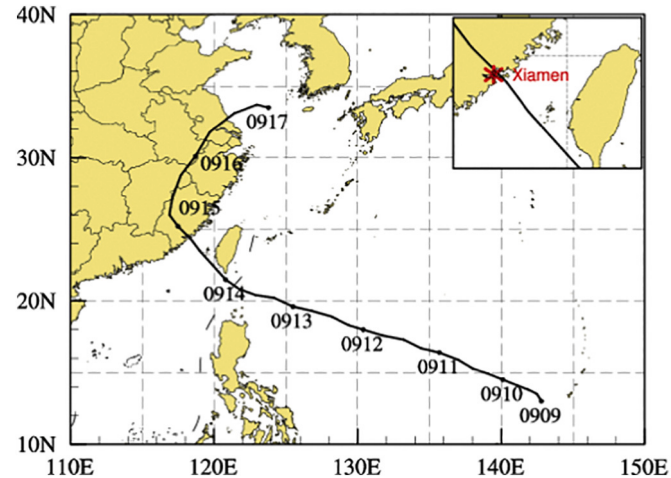


Fig. 1. Best-track positions of Typhoon Meranti, 09–17 September 2016.

Following this introduction, Section 2 provides an overview of Super Typhoon Meranti (2016). Section 3 describes the experimental designs of the mesoscale WRF model and diagnostic CALMET model, as well as the observational data used to validate the model simulation. Section 4 evaluates the performance of the CALMET simulations with differing horizontal resolution by validating the wind simulations against measurements. Section 5 examines the impact of different horizontal resolutions on the simulated near-surface wind fields from the perspective of slope angle in the two specified local regions. Finally, the main conclusions and a discussion are presented in section 6.

2. Super Typhoon Meranti (2016)

A detailed description of Super Typhoon Meranti can be found in Huang et al. (2019), and therefore only a brief introduction is presented here. Typhoon Meranti formed as a tropical depression near the island of Guam on 9 September 2016. It then intensified rapidly between 1200 UTC (Universal Coordinated Time) on 10 September and 1200 UTC on 12 September. At around 1900 UTC on 14 September, Meranti made landfall over Xiamen in Fujian Province (China). The best-track position of Meranti, shown in Fig. 1, is based on the China Meteorological Administration's best-track database (Ying et al., 2014).

Fig. 2 shows the evolution of the minimum sea level pressure (p_{\min}) and maximum total wind speed at 10 m (v_{\max}) as seen in the best-track analyses. The figure shows that Super Typhoon Meranti reached peak intensity at around 1200 UTC on 13 September, when p_{\min} was 890 hPa and v_{\max} was up to 75 m s^{-1} . At around 1900 UTC on 14 September, Meranti made landfall over Xiamen as a super typhoon with v_{\max} up to

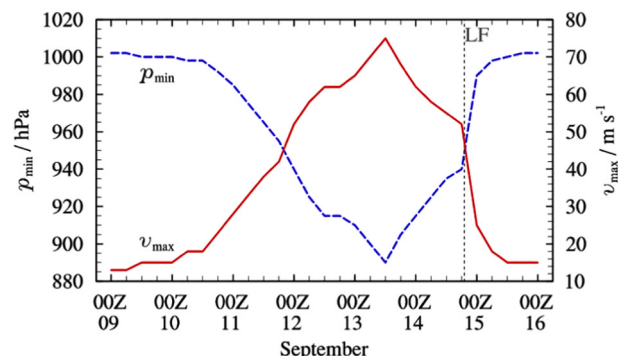


Fig. 2. Evolution of the minimum sea level pressure (p_{\min}) and maximum total wind speed at 10 m (v_{\max}) as seen in the best-track analyses. The vertical dashed line marks the time of landfall over Xiamen and Z denotes the time of UTC.

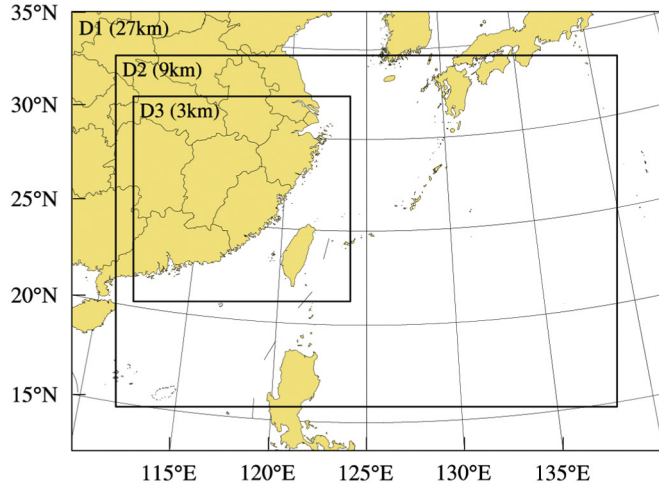


Fig. 3. Configuration of the three nested domains in the WRF model.

52 m s⁻¹, making it the strongest typhoon on record to affect Fujian Province. Subsequently, Meranti underwent rapid weakening during the following 6 h, in conjunction with increased vertical wind shear and decreased sea surface temperature (Li et al., 2019).

3. Experimental design

3.1. Mesoscale model

In the present study, Super Typhoon Meranti was simulated using the WRF/CALMET coupled system. The mesoscale model used here was the WRF model (version 3.8.1), which is a nonhydrostatic and fully compressible model designed to simulate or predict mesoscale atmospheric circulations (Skamarock et al., 2008). The WRF model was configured using three two-way nested domains with horizontal grid spacing of 27 (D1; mesh size: 135 × 203), 9 (D2; mesh size: 343 × 241) and 3 (D3; mesh size: 445 × 421) km (Fig. 3). In the vertical direction, there were 30 full Eta levels from the surface to 50 hPa with the lowest eight levels below 1 km to represent the planetary boundary layer. All nested domains were initialized as a “cold start” at 0000 UTC on 11 September 2016 and run for 120 h.

The physical parameterization schemes employed, which included the cumulus convection scheme, microphysical scheme, planetary boundary layer scheme, land surface model and radiation scheme, were the same as those described in Huang et al. (2019). The initial data and boundary conditions were obtained from the National Center for Environmental Prediction–Global Forecasting System analyses, which are produced four times a day with 1.0° horizontal grid spacing.

3.2. Diagnostic model

The diagnostic model used in this study was the CALMET model version 6.5, which is the meteorological component of the California Puff dispersion model (Scire et al., 1998). CALMET uses a two-step approach to compute wind fields. In Step 1, an initial guess wind field is adjusted for the kinematic effects of terrain, blocking effects and slope flows. In Step 2, an objective analysis procedure is applied to introduce observational data into the wind field derived in Step 1. In the configuration used for this study, the initial guess wind field was obtained from the gridded wind fields generated by the WRF innermost domain with 3-km horizontal grid spacing (D3 in Fig. 3). Because the procedure of objective analysis was not adopted, only the Step 1 wind field was of concern.

The topographic data were obtained from the National Aeronautics and Space Administration Shuttle Radar Topography Version 4 (SRTM

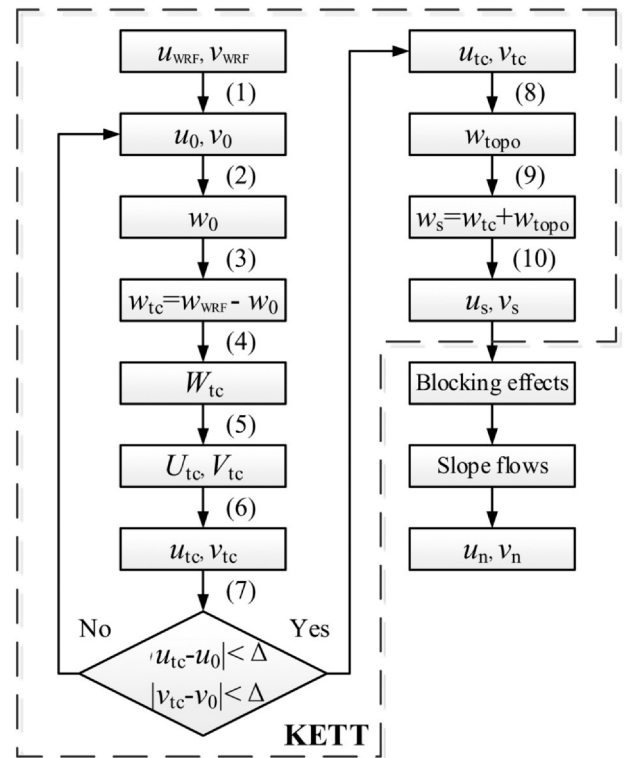


Fig. 4. Schematic of the “kinematic effects of terrain for typhoons” (KETT) approach. The pertinent variables are defined in the main text. Variables in lowercase are in Cartesian coordinates and variables in uppercase are in terrain-following coordinates.

V4) global 90-m digital elevation dataset, and the National Geomatics Center of China global 30-m land use data were adopted to determine the physical properties of the surface. Rzeszutek (2019) found that digital topographic data with 90-m horizontal accuracy were sufficient.

As suggested by Huang et al. (2019), the vertical velocity is computed only by orographic forcing and the initial guess wind field is assumed quasi-nondivergent. Consequently, the kinematic effects of terrain in CALMET can be applied only to atmospheric flows in stable conditions. In unstable conditions, such as typhoons and tornados, as vertical motion is commonly remarkable near the eyewall region, the present approach representing the kinematic effects of terrain, proposed by Liu and Yocke (1980), is inapplicable and must be improved.

3.2.1. Kinematic effects of terrain for typhoons

The present study adopted an improved approach named “kinematic effects of terrain for typhoons” (hereafter, KETT for short), which was first proposed by Tang et al. (2020). A schematic of KETT is presented in Fig. 4.

As shown in Fig. 4, (u, v, w) are wind components in Cartesian coordinates (x, y, z) and (U, V, W) are wind components in terrain-following coordinates (X, Y, Z) . Assuming that the effects of topography on the simulated wind fields are the same in both the WRF and the CALMET models with fixed horizontal grid spacing, the detailed steps of KETT can be explained as follows. (1) Assign the horizontal wind components of the WRF model (u_{WRF}, v_{WRF}) to the initial guess wind field in CALMET (u_0, v_0). (2) Compute the terrain-forced Cartesian vertical velocity (w_0) based on orographic forcing. (3) Assuming that the total vertical velocity of a typhoon in the WRF model (w_{WRF}) is equal to the sum of the terrain-forced vertical velocity (w_0) and the vertical velocity of its own vortex structure (w_{tc}), the value of w_{tc} can be obtained by subtracting w_0 from w_{WRF} . (4) Transfer w_{tc} in Cartesian coordinates to terrain-following coordinates (W_{tc}). (5) Compute the terrain-following horizontal wind components (U_{tc} and V_{tc}) using an

iterative divergence-minimization approach described by Goodin et al. (1980). (6) Transform U_{tc} and V_{tc} to Cartesian coordinates to obtain u_{tc} and v_{tc} . (7) Compute the differences between u_{tc} , v_{tc} and u_0 , v_0 . If the absolute differences are less than a threshold value (Δ), which was set to 0.01 m s^{-1} in this study, then u_{tc} and v_{tc} can be regarded as the horizontal wind components of typhoons undisturbed by orographic effects and the calculation can proceed to the following step. Otherwise, assign u_{tc} and v_{tc} are to the initial guess wind (u_0 and v_0) and repeat steps (2)–(7) until the absolute differences are less than the given threshold value Δ . (8) Compute the Cartesian vertical velocity (w_{topo}) forced by u_{tc} and v_{tc} . (9) Add w_{tc} to the value of w_{topo} to obtain the total vertical velocity under the action of typhoons (w_s). (10) Compute the Cartesian horizontal wind components u_s and v_s using the iterative divergence-minimization approach described by Goodin et al. (1980). The above 10 steps constitute the contents of KETT. After evaluation of KETT, the diagnostic module in CALMET then adjusts the initial guess wind for blocking effects and slope flows to produce the final wind field, i.e., u_n and v_n .

As shown in Fig. 4 of Tang et al. (2020), the systematic error of simulated wind fields near the typhoon center can be eliminated successfully using the KETT approach. Compared with the original approach proposed by Liu and Yocke (1980), the root mean square errors (RMSEs) of the 10-m wind speed and direction obtained using the KETT

approach can be reduced by 10.8% and 5.4%, respectively (Fig. 5 of Tang et al. (2020)), indicating that the KETT approach significantly improves the performance of the simulation of the near-surface wind field of typhoons.

3.3. Observational data

Assessment of the CALMET model was conducted for two specified regions named Shisun Mountain and Shishe Mountain (Fig. 5). As shown in Fig. 5(a), Shisun Mountain and Shishe Mountain are located to the left and right sides of the modeled typhoon track, respectively. There are two main peaks near the center of Shisun Mountain with elevations of 996 (northern peak) and 1067 m (southern peak) (Fig. 5(b)). The peak of Shishe Mountain, which is approximately 50 km north of Xiamen, is 1118 m above sea level (Fig. 5(c)). As Shisun Mountain and Shishe Mountain have double-peak and single-peak structures, respectively, and are surrounded by relatively flat areas, these two mountains were considered suitably representative of complex terrain for use in this study.

Distributed around Shisun Mountain and Shishe Mountain are 7 and 12 automatic surface observational stations, respectively. These automatic surface observational stations collected observational data during the passage of Super Typhoon Meranti. The wind speed and direction

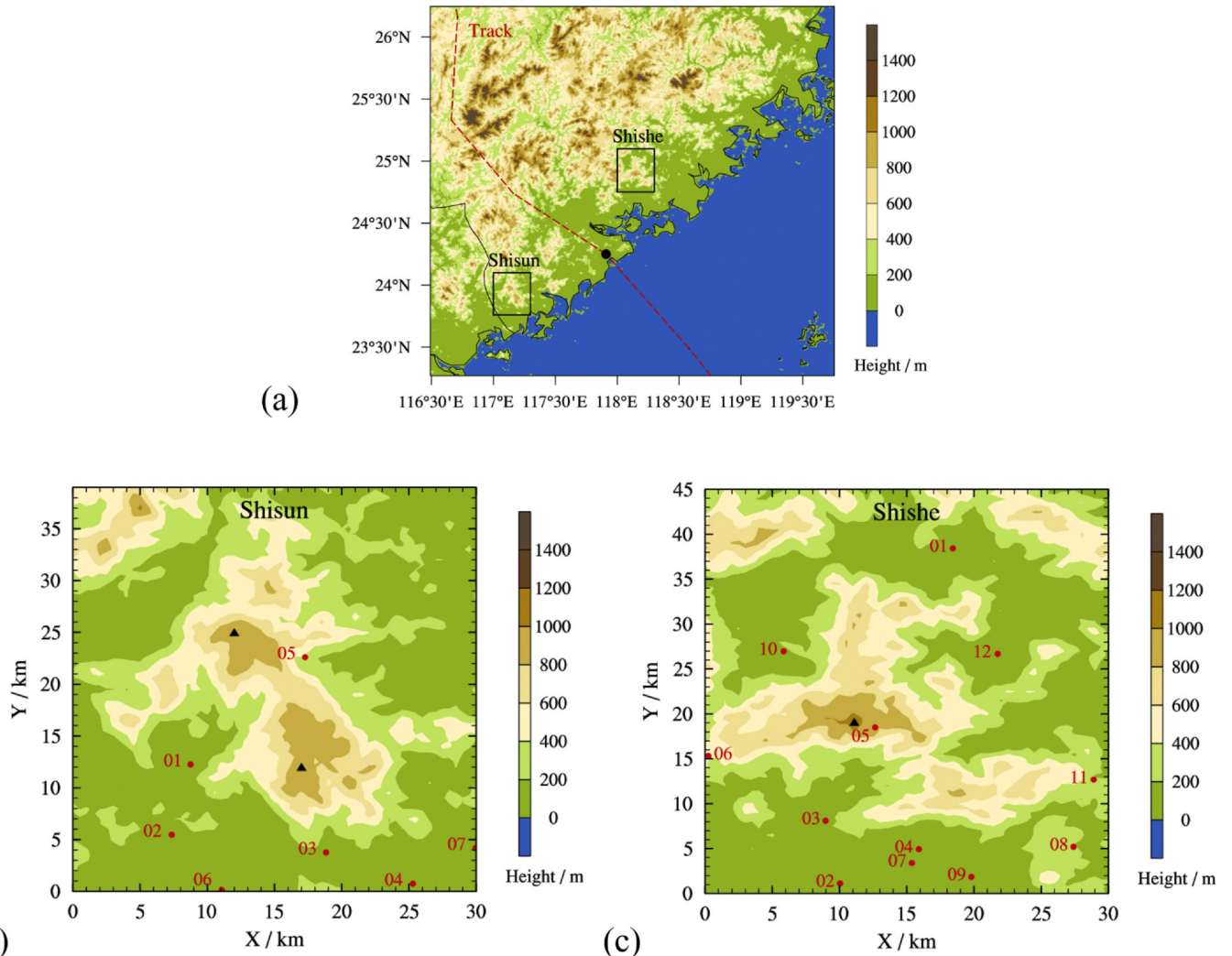


Fig. 5. Terrain of (a) the entire computational domain, (b) Shisun Mountain and (c) Shishe Mountain. The red dashed line represents the modeled track of Typhoon Meranti, the black dot represents the modeled position of the typhoon center at 0000 UTC on 15 September and the black triangles represent the mountain peaks. The shaded contours represent terrain elevation and the positions of the automatic surface observational stations are marked by red dots.

Table 1

Horizontal grid spacings and computational grid settings adopted for the five simulations in the CALMET model. The variables NX and NY denote the number of computational grids in the x and y directions, respectively.

Number	Horizontal grid spacing	Shisun Mountain		Shishe Mountain	
		NX	NY	NX	NY
1	3 km	10	13	10	15
2	1 km	30	39	30	45
3	500 m	60	78	60	90
4	250 m	120	156	120	180
5	100 m	300	390	300	450

were recorded as integrated averages at 5-min intervals at the height of 10 m above the surface. For this study, hourly averaged records were used as validation data. The observed time series data cover the period from 1200 UTC on 13 September to 0000 UTC on 16 September 2016.

3.4. Model simulations

The simulation results of typhoon winds are generally believed sensitive to model resolution. Therefore, it was considered reasonable to expect that slope angle would have an important effect on the simulated near-surface typhoon winds because the magnitude of the slope angle is closely related to model resolution. For this reason, five simulations with differing horizontal grid spacing were conducted for the Shisun Mountain and Shishe Mountain regions (Table 1).

In all calculations, the KETT approach was adopted and both blocking effects and slope flows were selected to adjust the wind field. In addition, the objective analysis procedure was not used.

4. Simulation results

The vortex evolution in the WRF simulation was as described in Huang et al. (2019). Generally, the level of agreement regarding typhoon track and intensity between the WRF simulation and the best-track analyses was remarkably good (Fig. 5 of Huang et al. (2019)). The initial guess wind field used in the CALMET model was provided by the gridded wind fields of the WRF model's innermost domain (D3 in Fig. 3).

First, the performance of the simulated near-surface wind fields in CALMET with differing horizontal resolution is evaluated by validating the wind simulations against measurements. Parameters including wind speed and direction derived from the CALMET simulations are compared with those recorded by the automatic observational stations distributed around Shisun Mountain and Shishe Mountain. Normalized Taylor diagrams and a table comparing the differences in 10-m wind speed (v_{10}) and direction (d_{10}) between the observations and the five CALMET simulations with horizontal grid spacing of 3 km, 1 km, 500 m, 250 m and 100 m at Shisun Mountain and Shishe Mountain are presented in Fig. 6 and Table 2, respectively. The reasonable performance of the WRF/CALMET coupled system is indicated by the relatively large correlation coefficient (> 0.4). Rife et al. (2004) suggested that a value of 0.4 is appropriate for representing a subjective cutoff for more skillful predictions. As shown in Fig. 6(a), the correlation coefficients of v_{10} are in the range 0.4–0.5 at Shisun Mountain and 0.55–0.65 at Shishe Mountain. Notably, the normalized standard deviations of v_{10} are overestimated at Shisun Mountain. As shown in Fig. 6(b), the correlation coefficients of d_{10} are in the range 0.7–0.8 at Shisun Mountain and 0.8–0.9 at Shishe Mountain. As shown in Table 2, the RMSEs of v_{10} and d_{10} are in the range 8.4–9.5 m s⁻¹ and 52°–60° for two mountains, respectively. Overall, the evaluation indicates that the 10-m wind speed and direction are reproduced more accurately at Shishe Mountain than at Shisun Mountain.

Now we focus on the surface performance of the five CALMET

simulations with differing horizontal resolution. Generally, there is no consistent tendency for the errors of v_{10} and d_{10} to decrease with increased horizontal resolution, which is consistent with the results found by Lu et al. (2012) and by Gonzalez et al. (2015). For the 10-m wind speed, the best and second-best outcomes at both places are found in the CALMET simulations with horizontal grid spacing of 500 and 250 m, respectively (Table 2). This is similar to the findings of Rzeszutek (2019), who reported that the best outcomes in terms of CALMET/CALPUFF accuracy were achieved with 400-m grid resolution. Theoretically, the use of a high-resolution grid should result in better description of the simulated airflow through more detailed representation of the topography and land cover (Rzeszutek, 2019). However, with the continuous reduction of horizontal grid spacing from 500 to 100 m, the RMSEs of v_{10} no longer decreases but increases by approximately 5% at both areas. This result is presumably because grid settings alone might not overcome the constraints of the model formulation, such as the physical representations in CALMET when the horizontal resolution is sufficiently high (Brode and Anderson, 2008). For the 10-m wind direction, the best outcome at Shisun Mountain is still found for the 500-m horizontal grid spacing (Fig. 6(b)). However, the simulations of d_{10} at Shishe Mountain appear to improve continuously with higher horizontal resolution.

Investigating the spatial distribution and variability of simulated wind fields is of great importance because one of the major benefits of the WRF/CALMET coupled system is the ability to capture the effects of finer-scale terrain on the wind field (Huang et al., 2019). Time series of 10-m wind speed (v_{10}) and direction (d_{10}) in the CALMET simulations and observed at selected stations at Shisun Mountain and Shishe Mountain are shown in Fig. 7. Based on the simulated vortex center and the radius of gale-force winds, these time series can be divided into three stages: (I) before, (II) during and (III) after the effects of the gale-force winds of Typhoon Meranti. According to the temporal variations of v_{10} and d_{10} of both the CALMET simulations and the observational stations, one station (Station 5) at Shisun Mountain and three stations (Stations 1, 4, 5) at Shishe Mountain were selected as suitable representatives with which to investigate the spatial variability of the simulated wind fields in the CALMET calculations with differing horizontal resolution. As shown in Fig. 5, Station 5 at Shisun Mountain is located approximately 5 km east of the north peak. At Shishe Mountain, Stations 1 and 4 lie to the north and south of the mountain, respectively, whereas Station 5 is located near the mountain peak.

Inspection of Fig. 7 suggests that the levels of agreement of v_{10} and d_{10} between the CALMET simulations and the observational stations are generally satisfactory. Before being affected by the gale-force winds of Typhoon Meranti (Stage I), the prevalent wind patterns are defined by northwest wind at Shisun Mountain and northeast wind at Shishe Mountain. A significant finding at Stage I is that there are relatively large differences of d_{10} among the five CALMET simulations at Station 5 at Shisun Mountain, and the best agreement of d_{10} at Stage I is in the experiment with 500-m horizontal grid spacing (Fig. 7(b)). When Shisun Mountain and Shishe Mountain are being affected by the gale-force winds of Typhoon Meranti (Stage II), the variations of v_{10} and d_{10} are much larger at Shishe Mountain than at Shisun Mountain. This is because Shishe Mountain was closer than Shisun Mountain to the typhoon center at around 0000 UTC on 15 September. Interestingly, significant spatial variation of v_{10} is detected around the peaks of Shishe Mountain. The maximum wind speed at Station 5 is up to 22 m s⁻¹, while the maximum value of v_{10} is 23 and 28 m s⁻¹ at Station 1 and Station 4, respectively. This is mainly because Station 5 is affected by blocking effects with a southwest wind, while Station 1 and Station 4 are hardly affected with a southeast or south wind (Huang et al., 2019). After being affected by the gale-force winds of Typhoon Meranti, a prominent feature at Stage III is the relatively large differences of v_{10} among the five CALMET experiments at all selected stations (Fig. 7(a), (c), (e), (g)), indicating that the 10-m wind speed appears sensitive to model resolution. This result is presumably due to the combination of

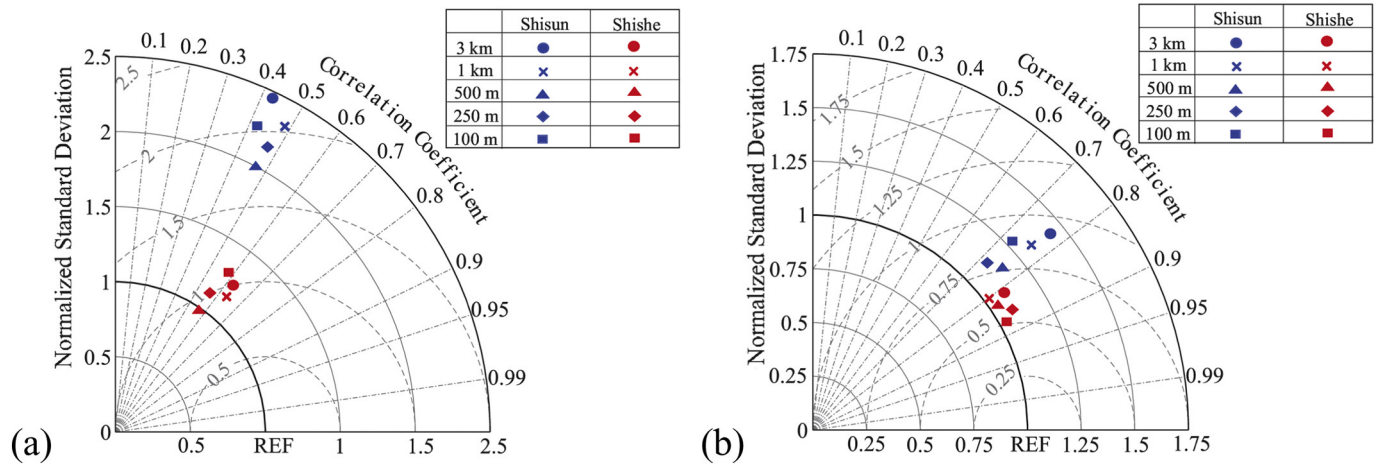


Fig. 6. Normalized Taylor diagrams showing differences of 10-m (a) wind speed (v_{10}) and (b) wind direction (d_{10}) between the observations and the CALMET simulations with horizontal grid spacing of 3 km, 1 km, 500 m, 250 m and 100 m at Shisun Mountain and Shishe Mountain. The period of the comparison extends from 1100 UTC on 14 September to 2000 UTC on 15 September 2016.

Table 2

RMSEs of 10-m wind speed (v_{10}) and wind direction (d_{10}) between the observations and the CALMET simulations with horizontal grid spacing of 3 km, 1 km, 500 m, 250 m and 100 m at Shisun Mountain and Shishe Mountain.

Horizontal grid spacing	RMSE (Shisun Mountain)		RMSE (Shishe Mountain)	
	v_{10} (m s^{-1})	d_{10} ($^\circ$)	v_{10} (m s^{-1})	d_{10} ($^\circ$)
3 km	9.46	60.23	8.71	54.64
1 km	9.22	58.74	8.66	54.39
500 m	8.83	55.68	8.41	53.75
250 m	9.04	56.99	8.54	53.04
100 m	9.27	59.27	8.96	52.00

kinematic effects of terrain and blocking effects as most part of typhoon Meranti was located over land during this stage. Moreover, there is no systematic difference in the behavior of d_{10} between the five CALMET simulations at Shishe Mountain (Fig. 7(d), (f), (h)), indicating that differing horizontal resolution in CALMET has little impact in terms of wind direction.

5. Slope angle

Having discussed statistical and site-specific comparisons of the near-surface wind field of the CALMET simulations with differing horizontal resolution, the main question is how to understand quantitatively the differences of the simulated near-surface winds over complex terrain during typhoon conditions. In terms of landscape morphology, finer-resolution complex terrain could be regarded as a combination of numerous “basic terrain units” that could be simplified as two-dimensional terrain with different slope angles, which could be the reason why the slope angle is a common and widely used parameter in analysis of the characteristics of the complex terrain (Park and Park, 2006; Zhong and Whiteman, 2008; Fang et al., 2019).

Conventionally, the slope angle is defined in geometry as the angle between a slope and a horizontal plane. In this paper, the “slope angle” of any given point is redefined as the angle between the slope along the wind direction and the horizontal plane to better analyze the near-surface winds over complex terrain. Fig. 8 shows a schematic illustrating the calculation of the wind-followed slope angle (α) of a given point A in a gridded numerical model. In this study, the terrain height of each grid point (h), horizontal spacing (L) and wind direction of the incoming flow (U) are used to calculate the slope angle by applying the central difference scheme. The uphill and downhill slope angles are defined as positive and negative values, respectively. Taking a east

wind as an example, the slope angle of grid point A is calculated using the following expression: $\alpha = (h_B - h_C)/L_{BC}$.

Fig. 9 shows box plots of slope angle (α) for the CALMET simulations with differing horizontal resolution during Stages I, II and III at Shisun Mountain and Shishe Mountain. In all stages, a prominent feature is that the distribution width of α generally increases with the increase of horizontal resolution from 3 km to 100 m, implying that the terrain is becoming increasingly complex and much steeper slopes are emerging in the finer-resolution terrain. As indicated by the whisker ends, the largest and smallest values of α in the double-peaked Shisun Mountain and single-peaked Shishe Mountain are similar and distributed mainly within the range of $[-5^\circ, 5^\circ]$, $[-10^\circ, 10^\circ]$, $[-15^\circ, 15^\circ]$, $[-20^\circ, 20^\circ]$ and $[-25^\circ, 25^\circ]$ for the CALMET simulations with horizontal grid spacing of 3 km, 1 km, 500 m, 250 m and 100 m, respectively. When Shisun Mountain and Shishe Mountain are being affected by the gale-force winds of Typhoon Meranti (Stage II), the mean values of α for the different horizontal resolutions are nearly equal to zero (Fig. 9(c) and (d)), suggesting that the distributions of the near-surface wind in the uphill direction and the downhill direction are almost the same. Nevertheless, in Stage I and especially in Stage III, the mean values of α are generally negative and they decrease with the increase of horizontal resolution (Fig. 9(e) and (f)), suggesting that finer-resolution terrain is likely to induce more downhill flows after being affected by the strong winds of Typhoon Meranti.

It should be noted that the topographic data used herein is the SRTM V4 dataset with horizontal resolution of 90 m, for which the averaged absolute elevation error is 6.4 m compared with GPS (Global Position System) data in north Greece (Mouratidis et al., 2010). In this research, the absolute elevation errors of observational stations range from 2.1 to 15.7 m at Shisun Mountain and 2.5 to 12.9 m at Shishe Mountain, with average values of 6.2 and 5.0 m, respectively. This fact indicates that the determination of computational height for the purpose of diagnostic modeling in CALMET with an accuracy of 5 m or more is not necessary. In other words, when the horizontal grid spacing is decreased to 100 m, the averaged absolute error of slope angle equals 2.86° . Furthermore, the absolute elevation error generally increases with the increase of slope angle, which is consistent with the results found by Szabo et al. (2015).

Fig. 10 shows box plots of the simulated 10-m wind speeds (v_{10}) with horizontal grid spacing of 3 km, 1 km, 500 m, 250 m and 100 m for differing slope angle (α) during Stages I, II and III at Shisun Mountain. As indicated by the frequency histogram, the vast majority of terrain is characterized with gentle slopes that are distributed within the range of $[-5^\circ, 5^\circ]$. Moreover, there are more downhill slopes than uphill slopes

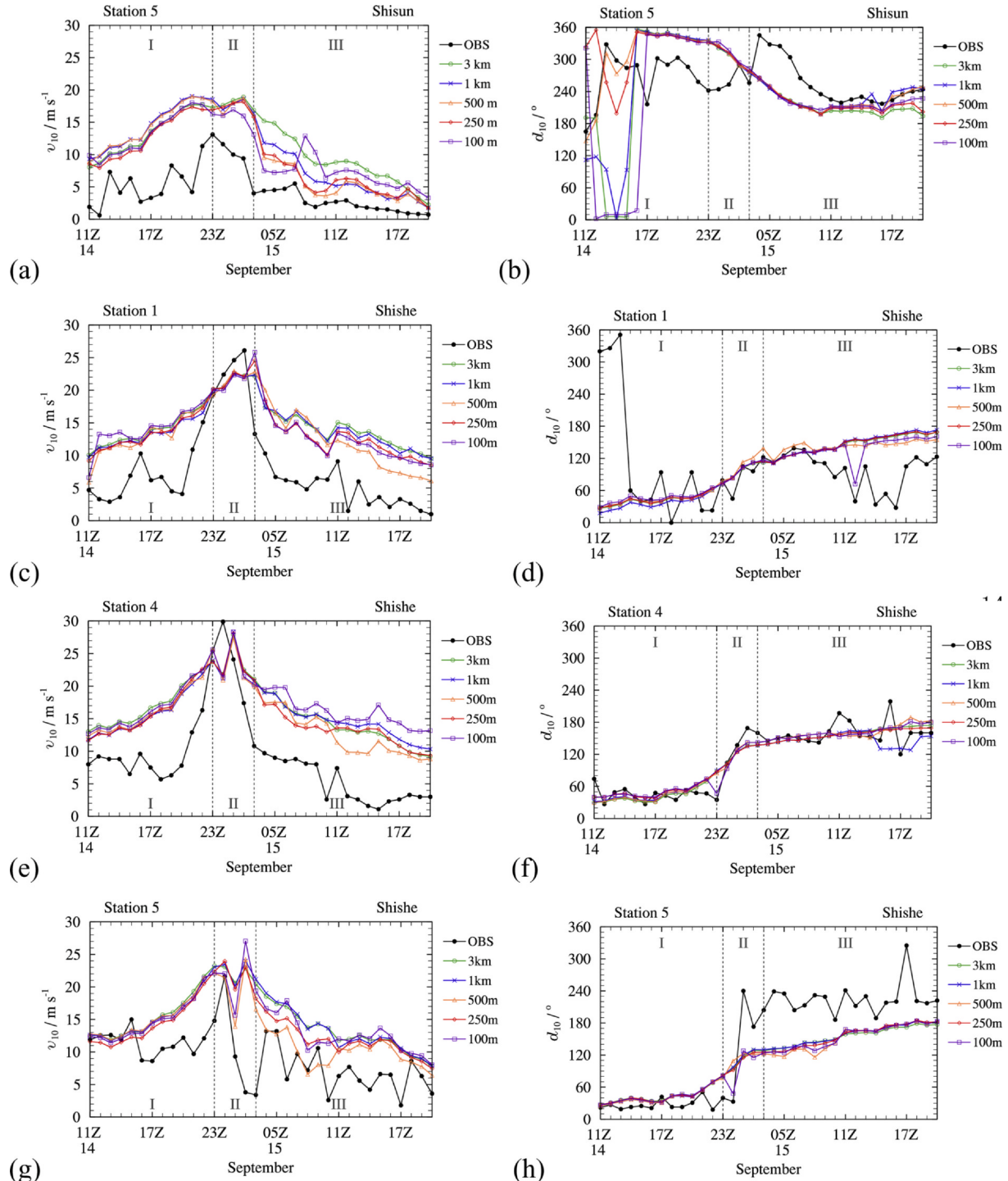


Fig. 7. Time series of 10-m wind speed (v_{10}) and direction (d_{10}) in the CALMET simulations with horizontal grid spacing of 3 km, 1 km, 500 m, 250 m and 100 m, and observed at (a, b) Station 5 at Shisun Mountain and (c, d) Station 1, (e, f) Station 4 and (g, h) Station 5 at Shishe Mountain. The Roman numerals denote the three stages, i.e., (I) before, (II) during and (III) after the effects of the gale-force winds of Typhoon Meranti.

at Shisun Mountain, which is rather remarkable in simulations with horizontal grid spacing of 3 km and 1 km. With the reduction of horizontal resolution, the finer-resolution terrain information will be gradually smoothed out in the coarser-resolution grids.

As shown in the first and third columns of Fig. 10, the 10-m winds are reasonably small at Shisun Mountain both before and after being affected by Typhoon Meranti. The mean values of v_{10} averaged during Stages I and III are approximately 10.2 and 4.7 m s^{-1} , respectively. It is noteworthy that a near-surface wind with a downhill slope is generally

larger than that with an uphill slope during these two stages, which can be explained by thermodynamic blocking effects and slope flows.

(1) Thermodynamic blocking effects.

In CALMET, thermodynamic blocking effects are parameterized using the term of the local Froude number (Allwine and Whiteman, 1985):

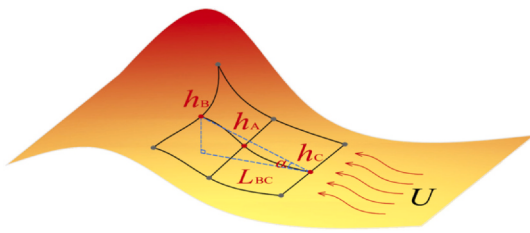


Fig. 8. Schematic illustrating the calculation of the wind-followed slope angle (α) at point A in a gridded numerical model. The variables h and L represent the terrain height and horizontal spacing, respectively, and U denotes the incoming flow.

$$Fr = \frac{V}{N\Delta h} \quad (4)$$

where Fr is the local Froude number, V is the local wind, N is the Brunt–Väisälä frequency and Δh is an effective obstacle height. If Fr is smaller than a critical Froude number and wind flows move uphill, CALMET adjusts the wind direction to be tangential to the terrain and it keeps the wind speed unchanged. Conversely, there is no adjustment of the wind flow if Fr is larger than the critical Froude number.

During Stages I and III, as the wind speed (V) is small and atmospheric stability (N) is large, the local Froude number (Fr) is smaller than the critical Froude number, and a net downslope flow that is tangential to the terrain is generated owing to the blocking effects (Huang et al., 2019).

(2) Slope flows.

In CALMET, the effects of slope flows are calculated based on the shooting flow parameterization of Mahrt (1982):

$$S = \left[\frac{Q_h g x \sin \alpha}{\rho c_p T (C_D + k)} \right]^{1/3} \left[1 - \exp \left(-\frac{x}{L_e} \right) \right]^{1/3}, \quad (5)$$

where S is the wind speed of the slope flow, Q_h is the local sensible flux, g is gravitational acceleration (9.8 m s^{-2}), x is the distance to the crest of the hill, α is the slope angle, ρ is the air density, c_p is the specific heat of air, T is the air temperature, C_D is the surface drag coefficient, k is the entrainment coefficient at the top of the slope flow layer and L_e is an equilibrium length scale. As shown in Eq. 5, S is correlated positively with local sensible flux (Q_h) and slope angle (α).

A prominent feature found by Huang et al. (2019) is that the flow moves downslope at night and upslope during daytime. Moreover, the downhill flow at night with a peak value of S of up to 2.5 m s^{-1} is stronger than the uphill flow during daytime (Fig. 14 of Huang et al. (2019)). Because almost all of Stage I and most of Stage III were during the night, it is reasonable to expect that the near-surface wind with a downhill slope would be larger than that with an uphill slope during these two stages, as explained by thermodynamic blocking effects and slope flows. In addition, the 10-m winds increase with the increase of slope angle in both uphill and downhill cases during Stages I and III, which is particularly obvious in the simulations with horizontal grid spacing of 250 and 100 m (Fig. 10(j), (l), (m), (o)).

When the radius of the gale-force winds of Typhoon Meranti is passing over Shisun Mountain, the prevalent wind direction turns rapidly from a north wind (Stage I) to a west wind (Stage II) in CALMET, which leads to an increase of the ratio of uphill flow in the simulations with horizontal grid spacing ranging from 1 km to 100 m. However, the ratio of uphill flow does not increase significantly for the simulation with 3-km grid spacing (Fig. 10(b)), which is presumably because the wind direction changes over the finer-resolution terrain have been smoothed out in the coarser-resolution grids. The 10-m winds during Stage II are larger than in the other two stages, with median values up to $17\text{--}18 \text{ m s}^{-1}$.

Another distinct feature during Stage II is that irrespective of whether an uphill or downhill case, the 10-m winds decrease with the increase of slope angle (Fig. 10(h), (k), (n)). This could be explained by the thermodynamic blocking effects and wind speed ratios of two-dimensional terrain (Fang et al., 2019). First, as wind speed (V) increases and atmospheric stability (N) decreases in the area of strong typhoon winds, the value of Fr exceeds the critical Froude number and therefore there is no adjustment of the wind flow owing to blocking effects in CALMET. Then, based on the numerical and experimental study of the aerodynamic characteristics around two-dimensional terrain with different slope angles by Fang et al. (2019), the wind speed ratios decrease with increased slope angle when the absolute value of α is larger than 10° in neutral or near-neutral stratification. According to the simulation results of Huang et al. (2019), atmospheric stability was near neutral near the surface when Typhoon Meranti made landfall over Xiamen. This explains why the largest wind occurs with small slope angle when α is distributed within the range of $[-5^\circ, 5^\circ]$ and why the 10-m winds decrease with increased slope angle when α becomes large during Stage II.

Fig. 11 shows box plots of the simulated 10-m wind speeds (v_{10}) with horizontal grid spacing of 3 km, 1 km, 500 m, 250 m and 100 m for differing slope angle (α) during Stages I, II and III at Shishe Mountain, i.e., the figure is the same as Fig. 10 but for Shishe Mountain. As indicated by the frequency histogram, the vast majority of terrain is characterized with gentle slopes, similar to that of the double-peaked structure of Shisun Mountain. However, the quantity of downhill slopes at Shishe Mountain is similar to or even slightly smaller than that of uphill slopes, which reflects a different distribution of slope angles relative to the inflow.

As indicated in the first and third columns of Fig. 11, the mean values of v_{10} averaged during Stages I and III are approximately 12.5 and 10.7 m s^{-1} , respectively, which are much larger than those at Shisun Mountain. This result is presumably because Shishe Mountain is located to the right of the typhoon track and is dominated by onshore winds. Conversely, Shisun Mountain is located to the left of the typhoon track and is dominated by offshore winds. Similarly, the downhill winds are generally larger than the uphill winds during Stages I and III, which could be explained by thermodynamic blocking effects and slope flows, as analyzed above.

After being affected by the gale-force winds of Typhoon Meranti (Stage III), v_{10} appears sensitive to model resolution (Fig. 7) and the minimum error of v_{10} is found in the experiment with 500-m horizontal grid spacing (Fig. 6). As indicated by the third column of Figs. 10 and 11, in comparison with v_{10} in the experiment with 500-m grid spacing, v_{10} in the experiments with 250- and 100-m grid spacing is distributed increasingly on steep slopes with absolute values of α larger than 15° . Moreover, v_{10} increases with slope angle in both uphill and downhill cases (Figs. 10(l), (o), 11(l), (o)). This result contradicts the findings of Fang et al. (2019), who reported that v_{10} decreases with slope angle when the absolute value of α is larger than 10° in neutral or near-neutral stratification. In CALMET, the differences of v_{10} among the five CALMET simulations are the result of the combined action of three physical representations: kinematic effects of terrain, blocking effects and slope flows. Therefore, the best outcome of v_{10} is found in the experiment with 500-m horizontal grid spacing presumably because the physical representations in CALMET are not applicable and the associated constraints of model formulation cannot be overcome by grid settings alone when the horizontal resolution is increased to 250 or even 100 m.

When Typhoon Meranti makes landfall over Xiamen, the prevalent wind direction at Shishe Mountain changes rapidly from a northeast wind (Stage I) to a southeast wind (Stage II), leading to an increase of the uphill flow for the simulations with horizontal grid spacing ranging from 3 km to 100 m. Meanwhile, the 10-m winds during Stage II are larger than in the other stages, with median values exceeding 20 m s^{-1} . Another obvious feature during Stage II is that irrespective of whether

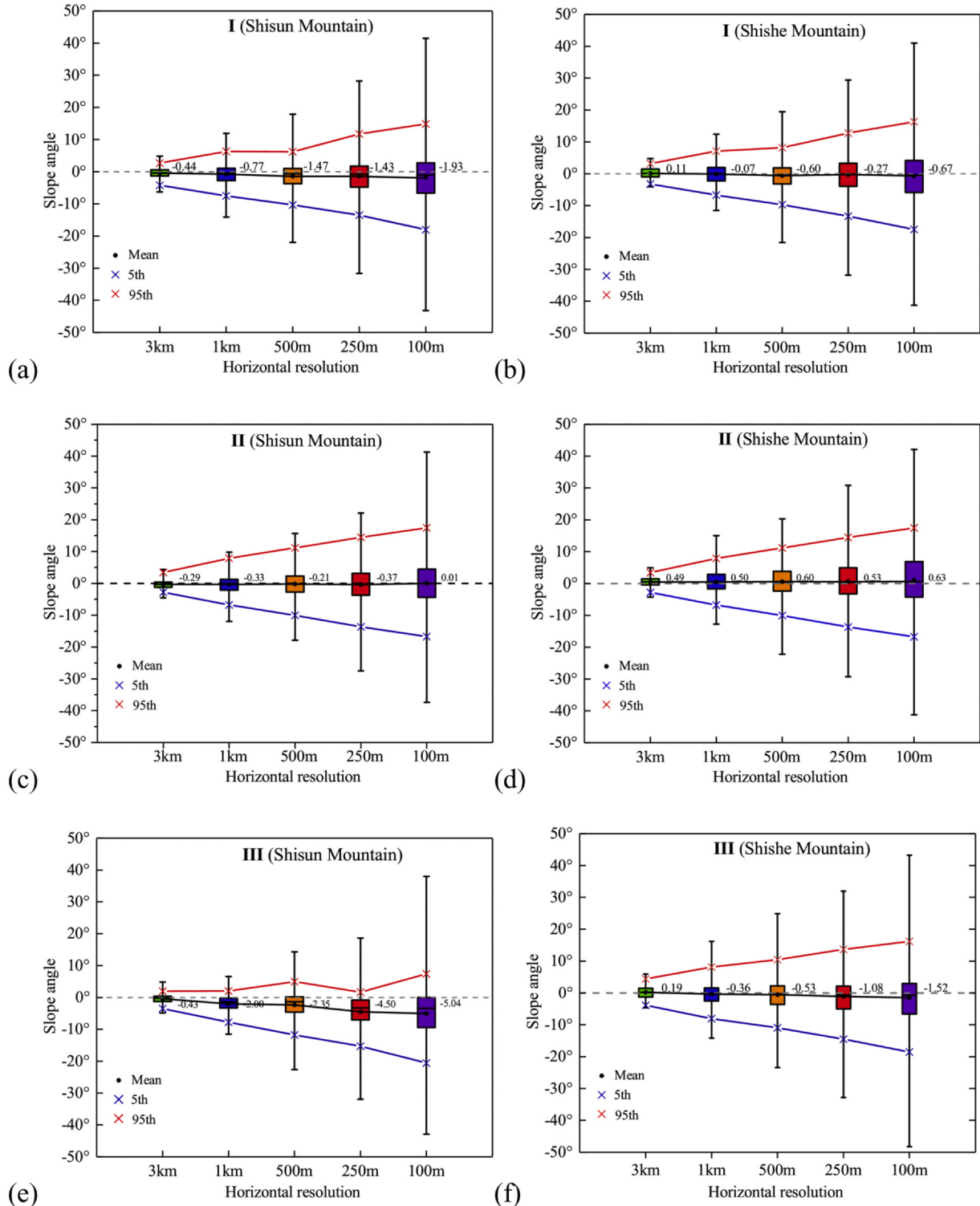


Fig. 9. Box plots of the slope angle (α) for the CALMET simulations with differing horizontal resolution during (a, b) Stage I, (c, d) Stage II and (e, f) Stage III at (a, c, e) Shisun Mountain and (b, d, f) Shishe Mountain. Central box area represents the 25th and 75th percentile values of the distribution, horizontal line inside the box is the median value, and whisker ends represent the smallest and largest values. Mean values are represented by black dots and the 5th and 95th percentile values are denoted by blue and red crosses, respectively.

an uphill or downhill case, the 10-m winds decrease with the increase of slope angle (Figs. 10(k), (n), 11(e), (h)). This is mainly because the wind speed decreases with slope angle when the absolute value of α is larger than 10° in neutral or near-neutral stratification, as highlighted by Fang et al. (2019).

Generally, the distributions of simulated near-surface winds with

different slope angles are resemble to each other in five CALMET simulations with differing horizontal grid spacing for both Shisun Mountain and Shishe Mountain during the passage of Typhoon Meranti, implying that the wind distributions with different slope angles are universal and insensitive to the location and model resolution.

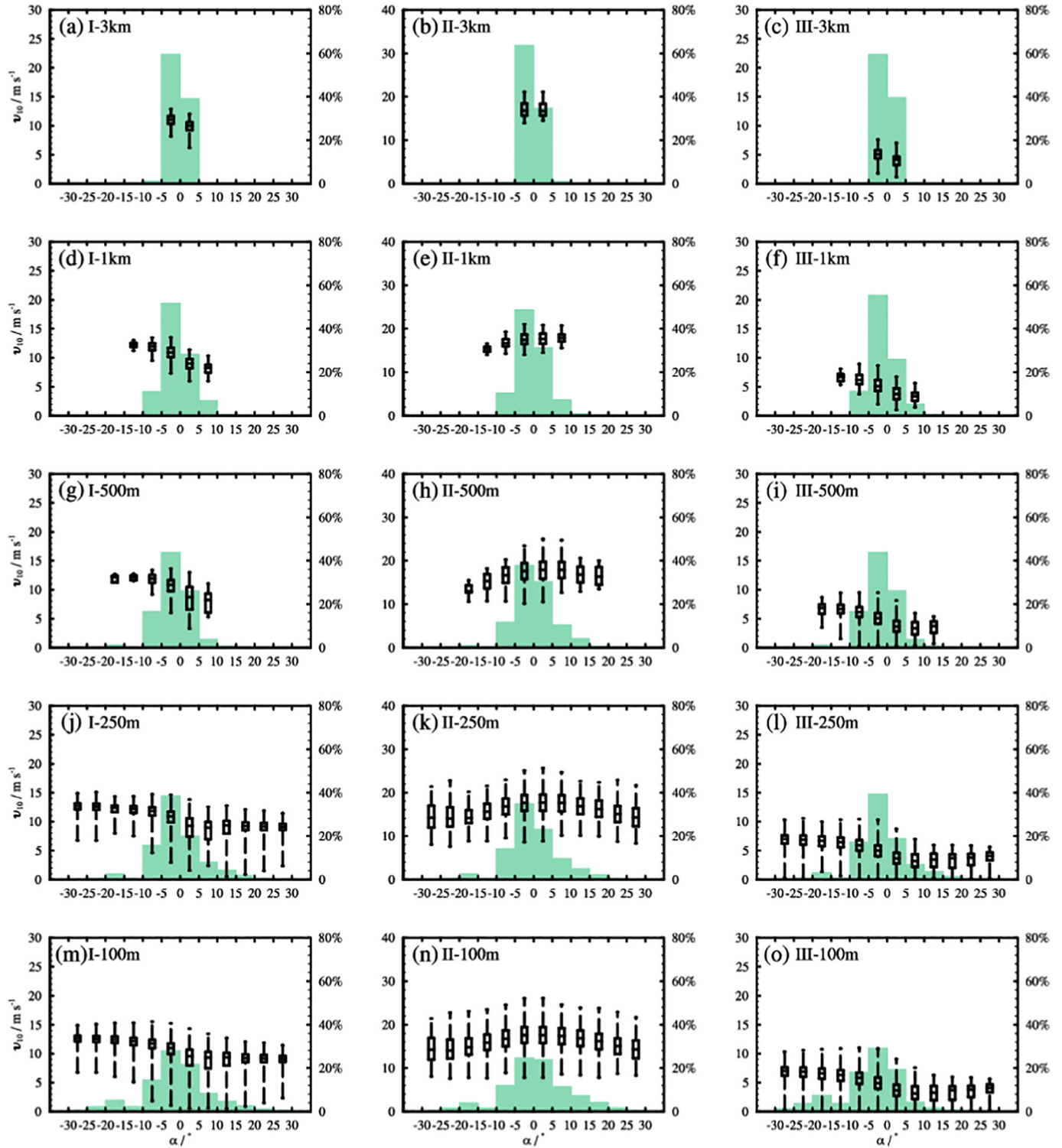


Fig. 10. Box plots of simulated 10-m wind speeds (v_{10}) with horizontal grid spacing of (a, b, c) 3 km, (d, e, f) 1 km, (g, h, i) 500 m, (j, k, l) 250 m and (m, n, o) 100 m for differing slope angle (α) during (left column) Stage I, (middle column) Stage II and (right column) Stage III at Shisun Mountain. Central box area represents the 25th and 75th percentile values of the distribution, horizontal line inside the box is the median value, and whisker ends represent the smallest and largest values. The green shaded areas denote the frequency histogram of slope angle.

6. Conclusions and discussion

This study examined the impact of horizontal resolution in the CALMET model on the simulated near-surface wind fields over complex terrain during the passage of Super Typhoon Meranti, which made landfall over Xiamen in Fujian Province (China) in 2016. The results of

a WRF simulation with horizontal grid spacing of 3 km coupled with five CALMET simulations with horizontal grid spacing ranging from 100 m to 3 km were discussed. As indicated by the reasonably large correlation coefficient (> 0.4) between the simulated and observed winds, the performance of the WRF/CALMET coupled system was generally satisfactory. Specifically, the correlation coefficients of 10-m

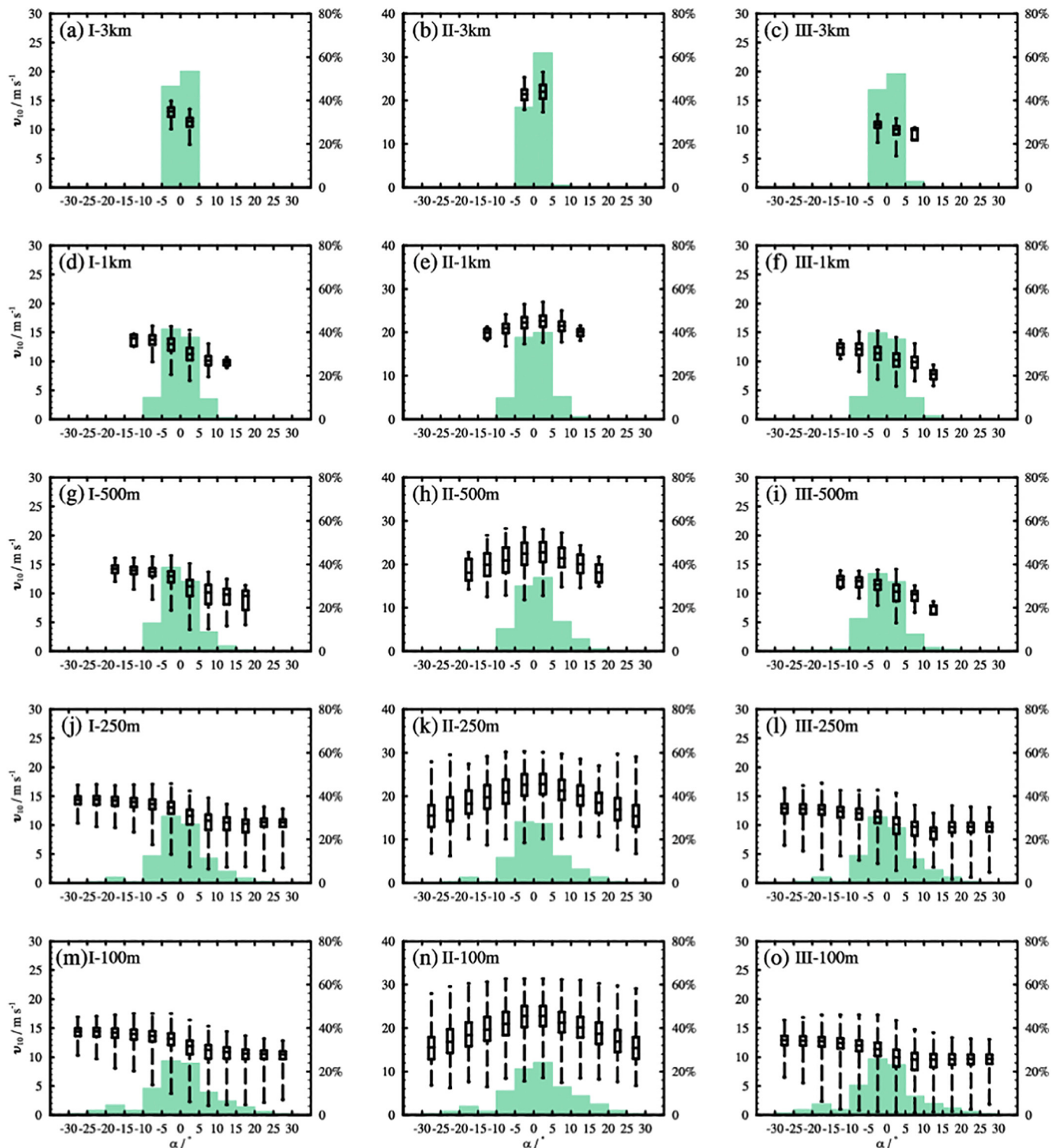


Fig. 11. Box plots of simulated 10-m wind speeds (v_{10}) with horizontal grid spacing of (a, b, c) 3 km, (d, e, f) 1 km, (g, h, i) 500 m, (j, k, l) 250 m and (m, n, o) 100 m for differing slope angle (α) during (left column) Stage I, (middle column) Stage II and (right column) Stage III at Shishe Mountain. Central box area represents the 25th and 75th percentile values of the distribution, horizontal line inside the box is the median value, and whisker ends represent the smallest and largest values. The green shaded areas denote the frequency histogram of slope angle.

wind speed were in the range of 0.4–0.5 at Shisun Mountain and 0.55–0.65 at Shishe Mountain, which is similar to the results found by Lu et al. (2012), i.e., correlation coefficients above 0.5 for both zonal and meridional wind components. However, the maximum wind observed by Lu et al. (2012) was less than $20 m s^{-1}$, which is a normal wind speed in non-typhoon conditions.

There was no consistent tendency for the errors of 10-m wind speed (v_{10}) and direction (d_{10}) to decrease with increased horizontal resolution. The best and second-best outcomes for v_{10} at both Shisun Mountain and Shishe Mountain were found in the CALMET simulations with horizontal grid spacing of 500 and 250 m, respectively, similar to the findings of Rzeszutek (2019), who reported that the best outcomes

of CALMET accuracy were achieved for 400-m grid spacing. After being affected by the gale-force winds of Typhoon Meranti, the results of v_{10} appeared sensitive to model resolution (Fig. 7(a), (c), (e), (g)) as most part of the typhoon was located over land, which is different to the findings of Chandrasekar et al. (2003), Lu et al. (2012) and Gonzalez et al. (2015) in non-tropical conditions. For the 10-m wind direction, the best outcome at Shisun Mountain was found with 500-m horizontal grid spacing; however, the simulations of d_{10} at Shishe Mountain appeared to improve slightly but continuously with higher horizontal resolution.

In this study, the conventional slope angle is redefined as the slope along the wind direction attempting to provide new perspective for quantitative evaluation of the impact of complex terrain with different horizontal resolutions on the simulated near-surface wind field. With the increase of horizontal resolution from 3 km to 100 m, the terrain became increasingly complex and much steeper slopes emerged in the finer-resolution terrain. Nevertheless, the majority of terrain remained characterized with gentle slopes distributed within the range of $[-5^\circ, 5^\circ]$. It should be noted that the topographic data used herein is SRTM3 V4 with resolution of 90 m, and the averaged absolute error of slope angle is 2.86° when the horizontal grid spacing is decreased to 100 m. As suggested by Fang et al. (2019), the physical representations in CALMET, which include the kinematic effects of terrain, blocking effects and slope flows, are not applicable after being affected by the gale-force winds of Typhoon Meranti (Stage III). Moreover, the associated constraints of model formulation cannot be overcome by grid settings alone when the horizontal resolution is increased to 250 or even 100 m.

Before and after being affected by the gale-force winds of Typhoon Meranti, the 10-m downhill winds were generally larger than the uphill winds, which can be explained by thermodynamic blocking effects and slope flows. While being affected by the gale-force winds of Typhoon Meranti, an increase of the ratio of uphill flow was detected owing to the rapid change of wind direction in the two areas. Moreover, the 10-m winds decreased with the increase of slope angle irrespective of whether an uphill or downhill case, which occurred primarily because the wind speed decreases with slope angle when the absolute value of the slope angle is larger than 10° in neutral or near-neutral stratification. Overall, the wind distributions with different slope angles are resemble to each other in all simulations with differing horizontal resolution for both Shisun and Shishe Mountains, implying that the wind distributions with different slope angles are universal and insensitive to the location and model resolution.

Declaration of Competing Interest

The authors declare that they have no known competing financial interests or personal relationships that could have appeared to influence the work reported in this paper.

Acknowledgements

This work was supported by the National Key R&D Program of China (No. 2018YFB1501104), Key Program for International S&T Cooperation Projects of China (No. 2017YFE0107700), the National Natural Science Foundation of China (No. 41805088), Natural Science Foundation of Shanghai (No. 18ZR1449100), Shanghai S&T Research Program (No. 19dz1200101), and State Key Laboratory of Disaster Reduction in Civil Engineering (SLDRCE19-A-05). We thank James Buxton MSc from Liwen Bianji, Edanz Group China (www.liwenbianji.cn.ac), for editing the English text of the original draft. Moreover, we are grateful also to two anonymous reviewers for their constructive comments on the original version of the submitted manuscript.

References

- Allwine, K.J., Whiteman, C.D., 1985. MELSAR: A mesoscale air quality model for complex terrain. In: Volume 1-Overview, Technical Description and user's Guide. Washington, Pacific Northwest Laboratory, Richland.
- Al-Yahyai, S., Charabi, Y., Gastli, A., 2010. Review of the use of Numerical Weather Prediction (NWP) models for wind energy assessment. Renew. Sust. Energ. Rev. 14, 3192–3198. <https://doi.org/10.1016/j.rser.2010.07.001>.
- Brode, R.W., Anderson, B., 2008. Technical Issues Related to use of the CALPUFF Modeling System for Near-field applications. U. S. EPA, OAQPS, Air Quality Modeling Group (C439-01), Research Triangle Park, NC.
- Chandrasekar, A., Philbrick, C.R., Clark, R., Doddridge, B., Georgopoulos, P., 2003. Evaluating the performance of a computationally efficient MM5/CALMET system for developing wind field inputs to air quality models. Atmos. Environ. 37, 3267–3276. [https://doi.org/10.1016/S1352-2310\(03\)00325-X](https://doi.org/10.1016/S1352-2310(03)00325-X).
- Chen, P., Yu, H., Xu, M., Lei, X., Zeng, F., 2019. A simplified index to assess the combined impact of tropical cyclone precipitation and wind on China. Front. Earth Sci. 13, 672–681. <https://doi.org/10.1007/s11707-019-0793-5>.
- Fang, P.Z., Zheng, D.Q., Li, L., Ma, W.Y., Tang, S.M., 2019. Numerical and experimental study of the aerodynamic characteristics around two-dimensional terrain with different slope angles. Front. Earth Sci. 13, 705–720. <https://doi.org/10.1007/s11707-019-0790-8>.
- Fierro, A.O., Rogers, R.F., Marks, F.D., Nolan, D.S., 2009. The Impact of Horizontal Grid Spacing on the Microphysical and Kinematic Structures of strong Tropical Cyclones simulated with the WRF-ARW Model. Mon. Weather Rev. 137, 3717–3743. <https://doi.org/10.1175/2009mwr2946.1>.
- Gioli, B., Gualtieri, G., Busillo, C., Calastrini, F., Gozzini, B., Miglietta, F., 2014. Aircraft wind measurements to assess a coupled WRF-CALMET mesoscale system. Meteorol. Appl. 21, 117–128. <https://doi.org/10.1002/met.1419>.
- Gonzalez, J.A., Hernandez-Garces, A., Rodriguez, A., Saavedra, S., Casares, J.J., 2015. Surface and upper-air WRF-CALMET simulations assessment over a coastal and complex terrain area. Int. J. Environ. Pollut. 57, 249–260. <https://doi.org/10.1504/IJEP.2015.074509>.
- Goodin, W.R., Mcrae, G.J., Seinfeld, J.H., 1980. An objective analysis technique for constructing three-dimensional urban-scale wind fields. J. Appl. Meteorol. 19, 98–108. [https://doi.org/10.1175/1520-0450\(1980\)019<0098:AOATFC>2.0.CO;2](https://doi.org/10.1175/1520-0450(1980)019<0098:AOATFC>2.0.CO;2).
- Gopalakrishnan, S.G., Marks, F., Zhang, X.J., Bao, J.W., Yeh, K.S., Atlas, R., 2011. The Experimental HWRF System: A Study on the Influence of Horizontal Resolution on the Structure and Intensity changes in Tropical Cyclones using an Idealized Framework. Mon. Weather Rev. 139, 1762–1784. <https://doi.org/10.1175/2010mwr3535.1>.
- Grell, G.A., Dudhia, J., Stauffer, D.R., 1995. A Description of the Fifth Generation Penn State/NCAR Mesoscale Model (MM5), Tech Note NCAR/TN-398 + STR. Boulder, CO, NCAR.
- Hu, J.L., Ying, Q., Chen, J.J., Mahmud, A., Zhao, Z., Chen, S.H., Kleeman, M.J., 2010. Particulate air quality model predictions using prognostic vs. diagnostic meteorology in Central California. Atmos. Environ. 44, 215–226. <https://doi.org/10.1016/j.atmosenv.2009.10.011>.
- Huang, S., Tang, S., Yu, H., Xue, W., Fang, P., Chen, P., 2019. Impact of physical representations in CALMET on the simulated wind field over land during Super Typhoon Meranti (2016). Front. Earth Sci. 13, 744–757. <https://doi.org/10.1007/s11707-019-0769-5>.
- Jackson, B., Chau, D., Gurer, K., Kaduwela, A., 2006. Comparison of ozone simulations using MM5 and CALMET/MM5 hybrid meteorological COOS fields for the July/August 2000 episode. Atmos. Environ. 40, 2812–2822. <https://doi.org/10.1016/j.atmosenv.2006.01.020>.
- Kanada, S., Wada, A., 2016. Sensitivity to Horizontal Resolution of the simulated Intensifying Rate and Inner-Core Structure of Typhoon Ida, an Extremely intense Typhoon. J. Meteorol. Soc. Jpn. 94A, 181–190. <https://doi.org/10.2151/jmsj.2015-037>.
- Li, M.X., Ping, F., Tang, X.B., Yang, S., 2019. Effects of microphysical processes on the rapid intensification of Super-Typhoon Meranti. Atmos. Res. 219, 77–94. <https://doi.org/10.1016/j.atmosres.2018.12.031>.
- Liu, M.K., Yocke, M.A., 1980. Siting of wind turbine generators in complex terrain. J. Energy. 4, 10–16. <https://doi.org/10.2514/3.62455>.
- Lu, Y.X., Tang, J.P., Wang, Y., Song, L.L., 2012. Validation of near-surface winds obtained by a hybrid WRF/CALMET modeling system over a coastal island with complex terrain. J. Trop. Meteorol. 18, 284–296. <https://doi.org/10.1175/JCLI-D-11-00322.1>.
- Mahr, L., 1982. Momentum balance of gravity flows. J. Atmos. Sci. 39, 2701–2711. [https://doi.org/10.1175/1520-0469\(1982\)039<2701:MBOGF>2.0.CO;2](https://doi.org/10.1175/1520-0469(1982)039<2701:MBOGF>2.0.CO;2).
- Majewski, D., 2009. HRM-user's guide, Deutschen Wetterdienstes (DWD). Offenbach, Germany.
- Morales, L., Lang, F., Mattar, C., 2012. Mesoscale wind speed simulation using CALMET model and reanalysis information: an application to wind potential. Renew. Energy 48, 57–71. <https://doi.org/10.1016/j.renene.2012.04.048>.
- Mortensen, N.G., Landberg, L., 1993. Wind Altas Analysis and Application Program (WASP) user's Guide. Riso National Laboratory, Roskilde, Denmark.
- Mouratidis, A., Briole, P., Katsambalos, K., 2010. SRTM 3 DEM (versions 1, 2, 3, 4) validation by means of extensive kinematic GPS measurements: a case study from North Greece. Int. J. Remote Sens. 31, 6205–6222. <https://doi.org/10.1080/01431160903401403>.
- Oleniacz, R., Rzeszutek, M., 2018. Intercomparison of the CALMET/CALPUFF Modeling System for selected Horizontal Grid Resolutions at a Local Scale: a Case Study of the MSWI Plant in Krakow, Poland. Appl. Sci. Basel. 8, 19. <https://doi.org/10.3390/app8112301>.

- Park, M.S., Park, S.U., 2006. Effects of topographical slope angle and atmospheric stratification on surface-layer turbulence. *Bound.-Layer Meteorol.* 118, 613–633. <https://doi.org/10.1007/s10546-005-7206-x>.
- Rife, D.L., Davis, C.A., Liu, Y.B., Warner, T.T., 2004. Predictability of low-level winds by mesoscale meteorological models. *Mon. Weather Rev.* 132, 2553–2569. <https://doi.org/10.1175/Mwr2801.1>.
- Rood, A.S., 2014. Performance evaluation of AERMOD, CALPUFF, and legacy air dispersion models using the Winter Validation Tracer Study dataset. *Atmos. Environ.* 89, 707–720. <https://doi.org/10.1016/j.atmosenv.2014.02.054>.
- Rzeszutek, M., 2019. Parameterization and evaluation of the CALMET/CALPUFF model system in near-field and complex terrain - terrain data, grid resolution and terrain adjustment method. *Sci. Total Environ.* 689, 31–46. <https://doi.org/10.1016/j.scitotenv.2019.06.379>.
- Scire, J.S., Robe, F.R., Fernau, M.E., Yamartino, R.J., 1998. A user's Guide for the CALMET Meteorological Model (Version 5). Earth Tech Inc, Concord, MA.
- Skamarock, W.C., Klemp, J.B., Dudhia, J., Gill, D.O., Barker, D.M., Duda, M.G., Huang, X.Y., Wang, W., Powers, J.G., 2008. A description of the advanced research WRF version 3, Tech. In: Note NCAR/TN-475+STR. Boulder, CO., NCAR.
- Sykes, R.I., Parker, S., Henn, D., Cerasoli, C., 1998. PC-SCIPUFF version 1.0, Titan ARAP Report no. 717, DTRA Technical Report. Titan Corporation, Alexandria, VA.
- Szabo, G., Singh, S.K., Szabo, S., 2015. Slope angle and aspect as influencing factors on the accuracy of the SRTM and the ASTER GDEM databases. *Phys. Chem. Earth* 83–84, 137–145. <https://doi.org/10.1016/j.pce.2015.06.003>.
- Tang, S., Huang, S., Yu, H., Gu, M., 2020. Impact of Kinematic Effects on simulated Near-Surface Wind Field of Landfall Typhoons. *J. Tongji Univ., Nat. Sci.* 48, 123–131. DOI: 10.11908/j.issn.0253-374x.19177. (in Chinese).
- US EPA, 2004. User's Guide for the AERMOD Meteorological Preprocessor (AERMET), EPA-454/B-03e002. U.S. Environmental Protection Agency, Research Triangle Park, NC.
- Yim, S.H.L., Fung, J.C.H., Lau, A.K.H., Kot, S.C., 2007. Developing a high-resolution wind map for a complex terrain with a coupled MM5/CALMET system. *J. Geophys. Res.-Atmos.* 112, D05106. <https://doi.org/10.1029/2006jd007752>.
- Ying, M., Zhang, W., Yu, H., Lu, X.Q., Feng, J.X., Fan, Y.X., Zhu, Y.T., Chen, D.Q., 2014. An overview of the China Meteorological Administration tropical cyclone database. *J. Atmos. Ocean Tech.* 31, 287–301. <https://doi.org/10.1175/Jtech-D-12-00119.1>.
- Zhong, S.Y., Whiteman, C.D., 2008. Downslope flows on a low-angle slope and their interactions with valley inversions. Part II: Numerical modeling. *J. Appl. Meteorol. Clim.* 47, 2039–2057. <https://doi.org/10.1175/2007jamc1670.1>.